Hydrology, environment (Pedology)

Soil porosity resulting from the assemblage of silt grains with a clay phase: New perspectives related to utilization of X-ray synchrotron computed microtomography

Porosité du sol résultant de l'assemblage de grains de la taille des limons avec une phase argileuse : nouvelles perspectives liées à l'utilisation de la microtomographie utilisant le rayonnement X d'un synchrotron

Olivier Rozenbaum [a,b,c], Ary Bruand [a,*,b,c], Emmanuel Le Trong [a,b,c]

[a] *UMR 7327, CNRS, université d'Orléans, institut des sciences de la terre d'Orléans (ISTO), 1A, rue de la Férollerie, 45071 Orléans cedex 2, France*
[b] *UMR 7327, CNRS/INSU, institut des sciences de la terre d'Orléans (ISTO), 45071 Orléans cedex 2, France*
[c] *UMR 7327, BRGM, institut des sciences de la terre d'Orléans (ISTO), BP 6009, 45060 Orléans, France*

A B S T R A C T

Understanding the assemblage of basic grains is essential for predicting many soil properties. X-ray synchrotron microtomography with a high resolution was used for visualisation and quantification of the assemblage of silt grains with a clay phase containing 20% of clays. The 3D computed image was analysed after appropriate segmentation by using: (i) autocorrelation functions which enables anisotropy discussion of the assemblage; (ii) chord distribution which gives information on the size distribution of the void and solid phases; and (iii) the Hoshen-Kopelman algorithm (6-connectivity) in order to label each void with a unique number and thus enabling discussion of the connectivity. Our results show that X-ray synchrotron microtomography enables a more accurate analysis of the assemblage of silt grains with a clay phase than with conventional methods. Thus, it showed the isotropy of the silt-clay assemblage in the studied soil material. The void and solid phase volumes were smaller than 80 and 120 μm in all directions, respectively. The mean distance between two interfaces was 6.9 and 13.4 μm for the void and solid phase, respectively. X-ray synchrotron microtomography of the soil material studied also showed that the voids resulting from the assemblage of the silt grains with the clay phase can be considered as fully connected in the studied dried materials.

© 2012 Académie des sciences. Published by Elsevier Masson SAS. All rights reserved.

R É S U M É

La compréhension du mode d'assemblage des grains élémentaires est essentielle pour la prédiction de nombreuses propriétés des sols. La microtomographie à haute résolution utilisant le rayonnement X d'un synchrotron a été utilisée pour analyser un matériau de sol correspondant à l'assemblage de grains de la taille des limons avec une phase argileuse contenant 20 % d'argile. L'image 3D reconstruite a été analysée après segmentation en utilisant : (i) des fonctions d'autocorrélation qui permettent de discuter le caractère anisotrope de l'assemblage ; (ii) des distributions de cordes qui donnent des informations

* Corresponding author.
   E-mail address: Ary.Bruand@univ-orleans.fr (A. Bruand).

sur la distribution de taille des vides et de la phase solide ; ainsi que (iii) l'algorithme de Hoshen-Kopelman (connectivité de 6), de façon à identifier chaque vide avec un nombre unique et ainsi discuter de la connectivité du réseau poreux. Nos résultats montrent qu'une telle microtomographie permet d'étudier le mode d'assemblage des grains de limon avec la phase argileuse avec plus de précision qu'avec les méthodes conventionnelles. Elle montre ainsi que l'assemblage étudié est isotrope et que les volumes de phase vide et solide sont plus petits que 80 et 120 µm dans toutes les directions, respectivement. La distance moyenne entre deux interfaces est de 6,9 et 13,4 µm pour la phase vide et la phase solide, respectivement. Enfin, l'analyse de la continuité des vides a révélé que les vides résultant de l'assemblage de grains de la taille des limons avec une phase argileuse pouvaient être considérés comme entièrement connectés à l'état sec dans le matériau étudié.

1. Introduction

Understanding the assemblage of basic grains is essential for predicting many soil properties (Bruand and Tessier, 2000; Coulon and Bruand, 1989; Lamotte et al., 1997a, b) and many studies have been conducted with grain mixtures varying in size distribution and mineralogy (e.g. Basile and d'Urso, 1997; Fiès and Bruand, 1990, 1998).

For decades, direct analysis of the assemblage of basic grains has been limited to 2D images of the assemblage taken with light and scanning electron microscopy. Recent developments of X-ray tomography have provided the possibility of starting 3D analysis of the assemblage of basic grains, but early images of the soil matrix remained limited by low resolution (Taina et al., 2008). Thus, X-ray tomography analysis of the elementary grain assemblage has long been limited to determine the attenuation of X-rays through the soil without the possibility of separating basic grains from the voids resulting from their assemblage. Recently, Schrader et al. (2007) studied by using X-ray tomography the differentiation of the assemblage of elementary particles around earthworm burrows but since the volume of the basic voxel was $3 \times 0.39 \times 0.39$ mm^3, the basic particles were not separated. With a much higher resolution of about 100 µm, Macedo et al. (1998) studied thin layers of soil clods but their discussion was also restricted to the variation of X-ray attenuation without the possibility of separating the solid phase and the related voids at the scale of the basic grains. Viggiani et al. (2004) studied deformation in fine-grained geomaterials under triaxal compression with a resolution of 14 µm and showed the development of cracks in the course of deformation. Because of both the fine texture and 14 µm resolution, they were not able to study the assemblage of basic particles. Using high-resolution computed tomography whose volume of voxels was $14.8 \times 13.5 \times 13.5$ µm^3, Lee et al. (2008) examined the size distribution of voids ranging from 10^3 to 10^9 µm^3 in volume within seals of a silt loam soil. Although the silt grains were recognisable on the images, their outlines and more generally the solid phase distribution, were highly fuzzy. Papadopoulos et al. (2009) used computed X-ray microtomography with a resolution of 8 µm to investigate the effects of organic and conventional management on soil aggregate stability and showed that intra-aggregate porosity would not affect stability. Peth et al. (2008) studied intra-aggregate porosity using X-ray synchrotron microtomography with a voxel volume of $3.2 \times 3.2 \times 3.2$ µm^3 or $5.4 \times 5.4 \times 5.4$ µm^3. The voids analysed were partly those resulting from the assemblage of the silt and sand grains with a clay phase, but resolution restricted their study. Sleutel et al. (2008) compared nano- and microfocus X-ray computed tomography for the visualisation of soil microstructure and soil organic matter. They discussed the void size distribution for equivalent diameters down to 1.7 µm but the analysis of void geometry remained limited. Gelard (2005) studied sand-clay mixtures with a clay content ranging from 5 to 25% using X-ray synchrotron microtomography with a resolution of 1.4 µm but the study of the 3D geometry of the voids was mainly limited to its skeletonization. Using microfocus X-ray tube computerized tomography, Tippkötter et al. (2009) reported a resolution down to 1 µm and investigated the presence of water in the macrovoids of undisturbed soils but did not study the voids related to the assemblage of the basic grains. Finally, Thieme et al. (2003) used nanotomography based on X-ray microscopy images with a resolution of about 0.045 µm in order to examine the microhabitat of bacteria and soil colloids. Their study was limited to colloidal flocculates extracted from soils and only 6 µm in size.

The objective of this study was to examine how X-ray synchrotron microtomography can lead to a better description of the void geometry resulting from the assemblage of the clay phase with silt grains. The resulting porosity was examined for a silt-clay mixture with 20% clay and the results show how X-ray microtomography provides new information on the 3-D assemblage of basic grains and resulting void geometry in soils which are usually discussed using data provided by indirect methods such as mercury intrusion curves, gas adsorption-desorption isotherms, and shrinkage curves (e.g. Braudeau and Bruand, 1993; Bruand and Prost, 1987; Bruand and Tessier, 2000; Nowamooz and Masrouri, 2010; Santos et al., 2011).

2. Material and methods

2.1. Sample preparation

The silt (10–50 µm) and clay (< 2 µm) fractions used in this study originated from the B horizon of a fine loamy, mixed, mesic, typic eutrochrept (Ould Mohamed et al., 1997). They were extracted from a suspension of the soil obtained by mechanical shaking in water (Attou et al.,

1998). The silt fraction was air-dried and the clay suspension was centrifuged to obtain a slurry of 0.7 g of water per gram of oven-dried clay (Attou et al., 1998). The clay fraction was primarily interlayered illite-smectite and secondary kaolinite, quartz and secondarily feldspars (Attou and Bruand, 1998). A soil material corresponding to a silt-clay mixture was obtained with 20% clay by manually mixing the clay paste and silt particles with a spatula. A clay content of 20% was chosen based on the high frequency of this clay content in loamy soils (Fiès and Bruand, 1990, 1998). The silt-clay mixture was placed in plastic rings 4 cm in diameter and 1 cm high, then equilibrated with a 10 hPa matric water potential using a pressure plate apparatus and finally air-dried (Attou et al., 1998).

After air-drying, the soil material was impregnated with a polyester resin as described by Bruand et al. (1996). A 700 μm thick section was prepared by grinding the resulting impregnated soil material. A sample in the shape of a matchstick $10,000 \times 700 \times 700$ μm^3 was prepared by cutting the 700 μm thick section with a diamond saw. It was then ground manually with sandpaper to blunt the edges and thus to obtain practically a cylindrical sample 700 μm in diameter and 10,000 μm high. Because of the high homogeneity of the soil material obtained (Attou et al., 1998), the prepared matchstick $10,000 \times 700 \times 700$ μm^3 in volume was considered as representative of the studied soil material.

2.2. Image acquisition

An image recorded by X-ray synchrotron microtomography was collected at 12 keV on the MS-X04SA-Tomo beam line of the Swiss Light Sources (http://sls.web.psi.ch/, Stampanoni et al., 2002). The cylindrical sample 700 μm in diameter was mounted on a vertical rotator on a goniometric cradle. Using successive rotations of the sample, 1500 projections corresponding to 1500 angular positions ranging from 0° to 180° were acquired by a 1024×1024 pixel digital camera. The outstanding quality of the beams enabled acquisition of images with a pixel resolution of 0.7 μm. The 700 μm diameter of the sample enabled to remain inside the field of view of the detector regardless of the angular position of the sample and thus to avoid reconstruction artefacts.

Acquisition required 120 min. A filtered back-projection algorithm was used to reconstruct horizontal slices 0.7 μm thick from the projections. These slices were apposed together to produce a 3D volume. Every pixel originating from a tomographic slice corresponds to a $0.7 \times 0.7 \times 0.7$ μm^3 voxel of the 3D image. The size of the entire dataset corresponding to a single 3D image was 1 Gigabyte (1024^3 voxels). Each voxel was characterised by its grey level which ranged from 0 to 255 for an 8-bit image, depending on the X-ray attenuation coefficient of the element. Thus, voids were rather dark and the solid phase was grey or white depending on its chemical composition (Fig. 1). The 3D visualisation of the solid and void phases was then possible at the scale of the assemblage of the basic grains thus enabling both the silt grains and clay phase together and the voids resulting from their assemblage to be visualised.
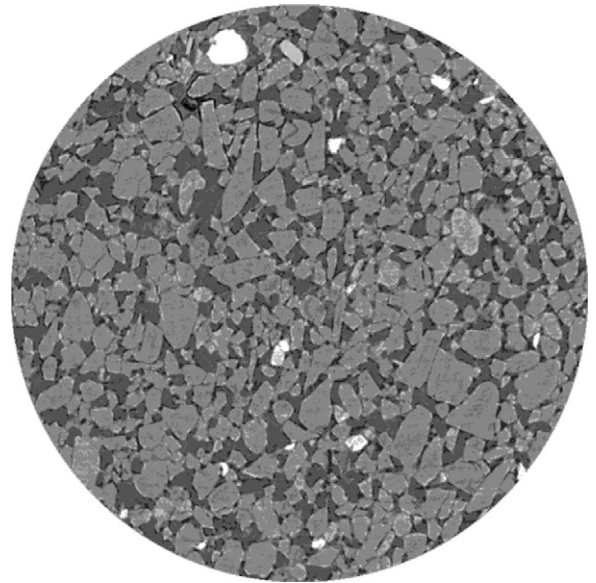

Fig. 1. 2D greyscale image of the soil material corresponding to a cross section of the 3D image recorded by X-ray synchrotron microtomography (radius = 400 pixels, i.e. 280 μm). Silt grains are in light grey and white, clay bridges and coating in light grey and voids in dark grey.

Fig. 1. Image 2D en niveaux de gris du matériau de sol correspondant à un plan transversal de l'image 3D enregistrée en microtomographie RX à l'aide d'un synchrotron (rayon = 400 pixels, i.e. 280 μm). Les grains de limon sont gris clair et blancs, les ponts et revêtements d'argile sont gris clair et les vides gris foncé.

2.3. Image segmentation

Image quantification requires proper segmentation of the solid and void phases. Although the images were well contrasted and the histogram was composed of two principal grey level domains, a direct threshold of the raw image was not sufficient to separate the voids and the solid particles (Fig. 2). This was related to the presence of noise that restricted the selection of a grey level as the limit
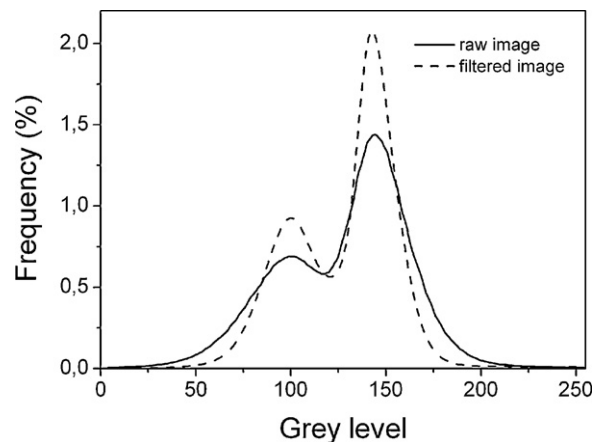

Fig. 2. Greylevel distribution corresponding to the 3D image recorded for the studied soil material.

Fig. 2. Distribution des niveaux de gris correspondant à l'image 3D enregistrée pour le matériau de sol étudié.

between the solid and void phases. Thus, after histogram equalisation (Acharya and Ray, 2005; Russ, 2002) to enhance their contrast, the signal-to-noise ratio (SNR) of the 8-bit images produced by the back-projection algorithm implemented at the SLS was 3.67. The SNR of an image is defined here as the ratio of its mean value to its standard deviation (Bushberg et al., 2006). Despite the two peaks associated with the grey values of the objects and the background being visible, noise still prevented correct segmentation (Fig. 2). After the application of a 3D mean filter with a kernel of $3 \times 3 \times 3$ voxels, the SNR reached 4.52. An optimum thresholding value of 112 was obtained using the classical method of Otsu (Otsu, 1979), which minimises the intra-class variance of the two populations of voxels. Comparison of ten segmented 2D images located approximately regularly along the 3D image with their respective raw 2D images showed that segmentation could be considered as satisfactory (Fig. 3). In the solid phase, however, it was not possible to separate silt grains and the clay phase forming the bridges and partially coating the silt grains.

The 3D segmented image recorded with the algorithms developed by Le Trong et al. (2008) was visualized by using VG-Studio software (http://www.volumegraphics.com/). It corresponded to the largest volume extractable from the 3D image obtained in grey levels. It had the shape of rod 588 μm in diameter and 716.8 μm high, i.e. 840 pixels in diameter and 1024 pixels in height, thus corresponding to a total of 5.7×10^8 voxels. This 3D rod-shaped volume was used to analyse the distribution of the solid and void phases in the sample.

2.4. Image analysis

The autocorrelation function, a spatial dependency of a porous medium (Cousin et al., 1996; Levitz and Tchoubar, 1992; Rozenbaum et al., 2007), can be interpreted as the probability of finding two randomly selected points that are both in the same phase. Let $\vec{x}$ be the position vector from an arbitrary origin and $\Psi(\vec{x})$ a density function defined as:

$$\Psi(\vec{x}) = 1 \tag{1}$$

if $\vec{x}$ belongs to the void, and

$$\Psi(\vec{x}) = 0 \tag{2}$$

if $\vec{x}$ belongs to the solid space. The autocorrelation function $R_Z(\vec{r})$ can be defined in order to have a normalised function (Rozenbaum et al., 2007):

$$R_Z(\vec{r}) = \frac{< (\Psi(\vec{x}) - \phi)(\Psi(\vec{r} + \vec{x}) - \phi) >}{\phi(1 - \phi)} \tag{3}$$

with ϕ the porosity which was computed according to the following relationship:

$$\phi = \frac{V_v}{V_v + V_s} \tag{4}$$

with V_v and V_s, the volume of the void and solid phases, respectively. For the studied 3D image, V_v and V_s were the numbers of voxels corresponding to the void and solid

phases, respectively. The angle brackets mean average volume over the spatial coordinates $\vec{x}$. For an isotropic medium with $r = |\vec{r}|$:

$$R_Z(\vec{r}) = R_Z(r) \tag{5}$$

which indicates that the autocorrelation function depends only on distance. Otherwise, the one-dimension autocorrelation functions for $\vec{r}$ parallel to the Ox, Oy or Oz axis (Ox, Oy, Oz defining an orthogonal reference, and Oz being perpendicular to the plastic ring plane used to prepare the soil material in the pressure plate apparatus), respectively denoted R_{Zx}, R_{Zy} and R_{Zz} provides information on anisotropy. Void anisotropy is in fact revealed as a disparity between the one-dimensional autocorrelation functions along different directions (Biswal et al., 1999; Frykman and Rogon, 1993).

Another characteristic length scale is the correlation length (L), defined as the integral of the autocorrelation function and represents a length scale characteristic of the spatial structure (Ioannidis et al., 1996):

$$L = \int_0^\infty R_Z(r) dr \tag{6}$$

For anisotropic materials, L_x, L_y and L_z are defined according to R_{Zx}, R_{Zy} and R_{Zz}.

Chord distributions are stereological tools used to describe the interface between void and solid phases (Rozenbaum et al., 2007). Chord distribution gives the probability to have a chord length between r and $r+dr$. Chord distribution can be calculated either for voids ($f_v(r)$ is called the void chord distribution) or for solids ($f_s(r)$ is called the solid chord distribution). Furthermore, the first moment of $f_v(r)$ (called l_v) and the first moment of $f_s(r)$ (called l_s) are defined as:

$$l_v(r) = \int r\, f_v(r) dr \tag{7}$$

and,

$$l_s(r) = \int r\, f_s(r) dr \tag{8}$$

The values of l_v and l_s can be used as estimators of the mean size of the void and solid phases.

Finally, topology of the voids can be analyzed for the 3D image of the void distribution. The Hoshen-Kopelman algorithm (6-connectivity) was used to label each void with a unique number (Hoshen and Kopelman, 1976). It is a simple and efficient cluster identification algorithm enabling identification of connected clusters on a lattice (Stauffer and Aharony, 1992). We determined the number of voxels for each cluster and the basic topological properties that are: the number of isolated voids (N), the number of redundant connections (C) within the void space and the number of completely enclosed cavities (H) (Vogel et al., 2002). In other words, C represents the number of bonds that can be removed without creating an additional isolated cluster. The Euler-Poincaré characteristic ε_V was then computed as:
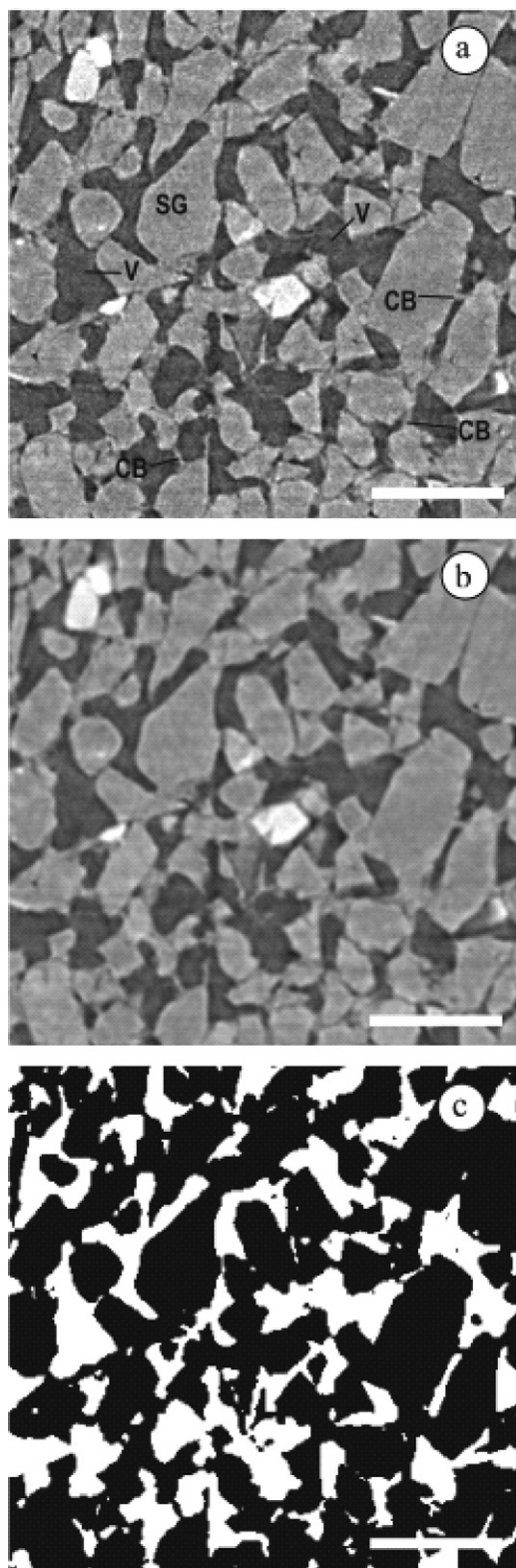
$$\varepsilon_V = N - C + H \tag{9}$$

Fig. 3. 2D greyscale image (280 × 280 pixels; bar length = 20 μm) extracted from the image shown in Fig. 1 and showing the voids (V), the clays bridges (CB) between the silt grains (SG) (a), the corresponding filtered (b) and binary image (c).

Fig. 3. Image 2D en niveaux de gris (280 × 280 pixels ; longueur de l'échelle = 20 μm) extraite de l'image présentée Fig. 1 et montrant les vides (V), les ponts d'argile (CB) entre les grains de limon (SG) (a), l'image correspondante filtrée (b) et binaire (c).

using the algorithm established by Vogel (2008). For the topology of porous media such as soils, the quantity H is of minor importance since solid grains or particles completely surrounded by voids are infrequent, thus H is set to be zero in Eq. (9) (Vogel et al., 2002). As this characteristic is related to the total volume (V, in units of voxels) and in order to compare images with different sizes, the specific Euler-Poincaré number was defined as:

$$\chi_\nu = \varepsilon_V / V \tag{10}$$

Thus, the specific Euler-Poincaré number can be considered as a measure of connectivity; the higher this number, the less connectivity would be expected.

For all the characteristics (porosity, Euler-Poincaré number, chord length distributions) presented here, a 3D mask (cylinder with a given radius and a given height or parallelogram) was applied on the 3D image. Hence, each voxel exterior to this mask was ignored. In other word, considering a void cut by the mask, only the part of the void inside the mask was taken into account for the calculated characteristic. This bit of void could be: (i) isolated if totally surrounded by grains (in fact demarcated by the grains and by the mask); or (ii) connected to other voids located deeper within the mask (and then connected). Note that these voids cut by the mask were not considered as interconnected by the exterior of the mask. They could be connected only if a path (inside the mask) constituted of voids linked them. This is obviously respectively the same for a grain.

An error is necessarily made and obliges to take the biggest volume as possible to minimize this artifact (notion of REV).

3. Results and discussion

3.1. Morphology of the assemblage

The 2D images in grey levels extracted from the 3D image showed a close packing of the silt grains and the presence of bridges between them (Fig. 3a). These bridges are 5–20 μm long and 2–5 μm thick and correspond to the bridges composed of clay particles shown by Attou et al. (1998) on backscattered electron scanning images. These bridges are responsible for the hardness increase of soils in the field when they dry (Attou et al., 1998; Lamotte et al., 1997a, b). The voids between silt grains were described as lacunar voids by Fiès and Bruand (1998) because they are not filled by the clay phase. According to the results of Attou et al. (1998) which were recorded by using mercury porosimetry, they are mainly accessible to void necks with equivalent void diameters ranging from 0.5 to 5 μm.

After segmentation, the 2D tomographic images clearly showed the 2D geometry of voids (Fig. 3b, c). Accurate comparison of the solid phase distribution on 2D grey scale images (Fig. 3a), their corresponding 2D filtered images
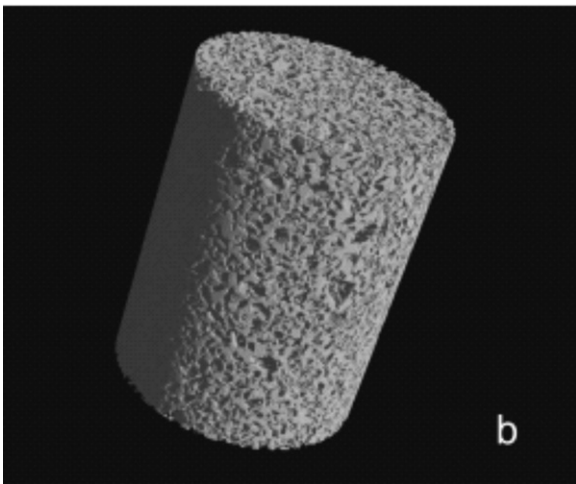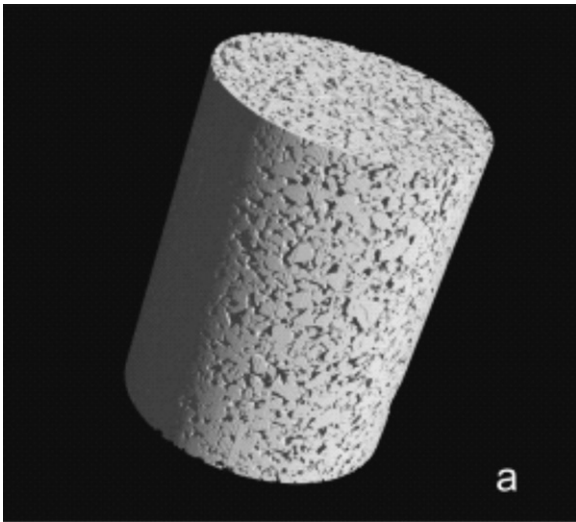
Fig. 4. 3D binary image (radius = 420 pixels, height = 1024 pixels) of the studied soil material (a: visualisation of the solid phase and b: void phase).

Fig. 4. Image binaire 3D (rayon = 420 pixels, hauteur = 1024 pixels) du matériau de sol étudié (a : visualisation de la phase solide et b : de la phase vide).

Fig. 5. 3D binary image ($200 \times 200 \times 200$ voxels) of the studied soil material (a: visualisation of the solid phase and b: void phase).

Fig. 5. Image binaire 3D ($200 \times 200 \times 200$ voxels) du matériau de sol étudié (a : visualisation de la phase solide et b : de la phase vide).

(Fig. 3b) and finally binary 2D images (Fig. 3c), showed that the clay bridges 2–5 μm thick are still present on the 3D binary images after image segmentation. The segmented reconstructed images of the void and solid phases corresponding each to a cylinder 294 μm in radius and 717 μm long are shown on Fig. 4. The 3D-distribution of the solid and void phases in the studied soil material can be seen more easily on smaller cubic 3D-images $200 \times 200 \times 200$ voxel cubes (i.e. $140 \times 140 \times 140$ μm³) in volume, as shown in Fig. 5.

Detailed observation of the void morphology enabled identification of the voids which correspond to the elementary lacunar voids described by Attou et al. (1998) in the same soil material and more widely in soils by Fiès and Bruand (1998). However, 3D-images showed that the lacunar voids are far from the roughly ovoid voids
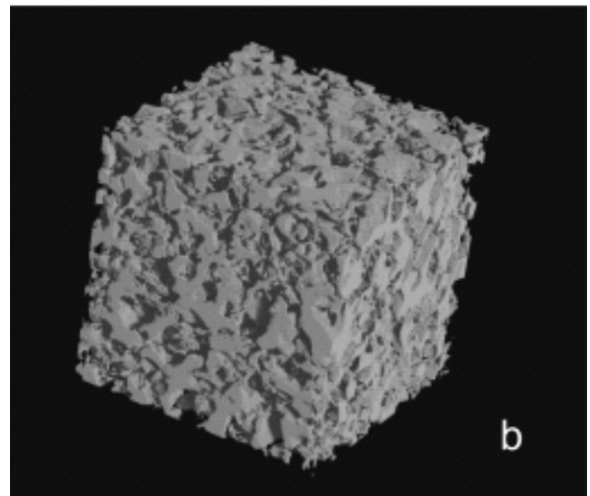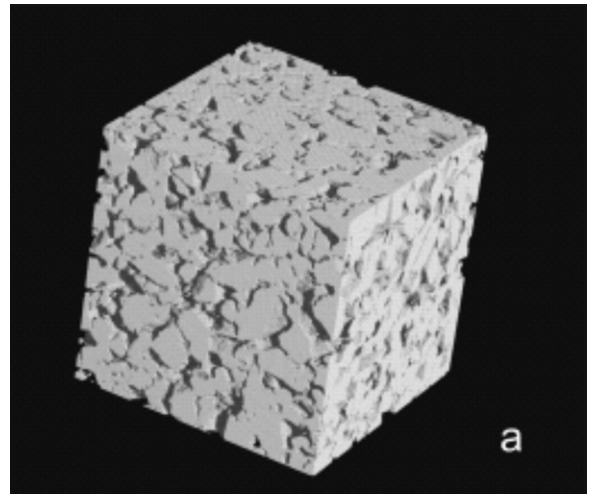
resulting from the packing of the silt particles with the clay phase and networked thanks to void necks as earlier indicated by both 2D backscattered scanning electron images and mercury porosimetry (Attou et al., 1998, Fiès and Bruand, 1998). Indeed, morphological observation of the connections of the elementary lacunar voids with the surrounding elementary lacunar voids showed a much more continuous void size distribution than in a lacunar void as usually described (Fiès and Bruand, 1998) (Fig. 6).

3.2. Porosity

We computed ϕ for 3D cubic image sizes ranging from 79×10^2 to 50×10^7 voxels (Fig. 7). For a given cubic image size, the porosity was computed, the volume of measure was shifted (non overlapping cubes) and the porosity was computed again. This was repeated until the cubic image size scanned the whole image. For the smallest 3D image
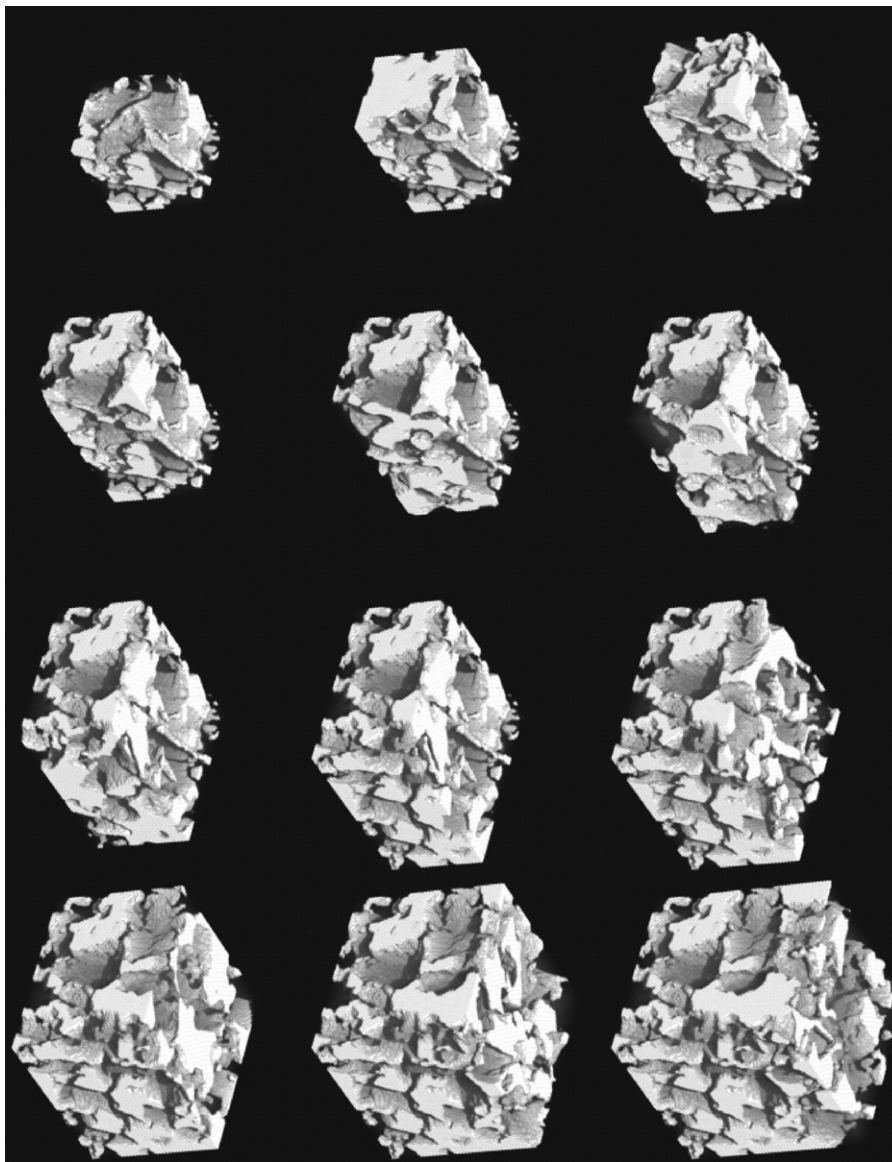
Fig. 6. Successive 3D images showing a single lacunar pore (void shown as solid, left top corner, $70 \times 70 \times 60$ voxels) and then its local surrounding environment by adding successively lateral connected lacunar pores up to a 3D image $120 \times 120 \times 120$ voxels in size (right bottom corner).

Fig. 6. Images 3D successives montrant un pore lacunaire isolé (phase vide représentée sous la forme de solide, image en haut à gauche, $70 \times 70 \times 60$ voxels) et son environnement local en ajoutant successivement les pores lacunaires latéraux, connectés jusqu'à une image 3D de $120 \times 120 \times 120$ voxels de taille (image en bas à droite).

size, ϕ varied considerably and thus converged toward a limit when the 3D image size increased. This limit was reached when the 3D image size was about 10^7 voxels ($343 \times 10^5 \ \mu m^3$). This image size can be considered as the representative elementary volume to investigate porosity for the studied material, the representative elementary volume being the sample volume over which the porosity can be considered as a constant.

Porosity computed for the studied entire rod volume was 0.337 (Table 1) and smaller than the porosity determined using bulk density measurements (0.359) by

Attou and Bruand (1998) on the same soil material. This difference was related to voids resulting from the assemblage of the clay particles within clay coatings and bridges (Fiès and Bruand, 1998) and not taken into account in image analysis because they were smaller than the voxel size ($0.7 \times 0.7 \times 0.7 \ \mu m^3$). The porosity determined by 3D-image analysis in this study (i.e. 0.337) corresponded actually to the voids between the silt grains and described as lacunar voids by Fiès and Bruand (1998) and was similar to its value determined by using mercury porosimetry (0.335) by Attou and Bruand (1998) on the same material.
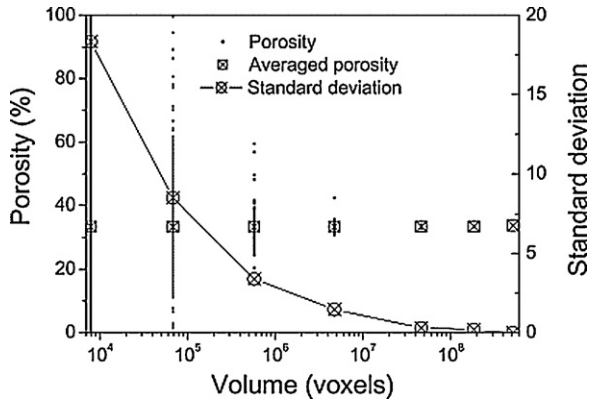
Fig. 7. Porosity, averaged porosity and standard deviation according to the size of the 3D region of interest in the entire 3D image.

Fig. 7. Porosité, porosité moyenne et écart-type en fonction de la taille de la région d'intérêt 3D dans l'ensemble de l'image 3D.
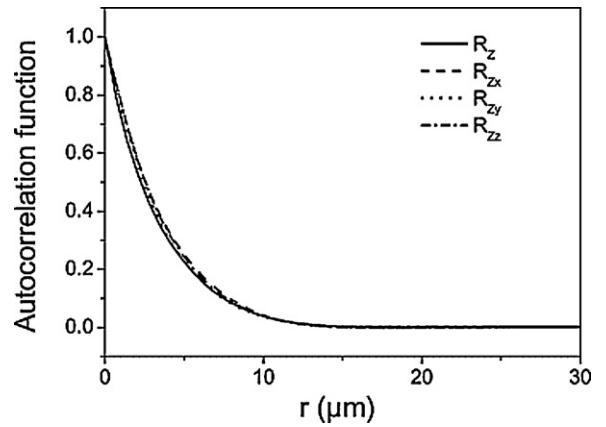

Fig. 8. Autocorrelation functions recorded for the studied soil material.

Fig. 8. Fonctions d'autocorrélation enregistrée pour le matériau de sol étudié.

3.3. Void geometry

The autocorrelation functions R_{zx}, R_{zy} and R_{zz} and the average value R_z recorded showed a decreasing behaviour without any oscillation, corresponding to a non-correlated medium (Fig. 8). In addition, no particular disparity was observed on the images for the one-dimensional autocorrelation functions along the orthogonal x-, y-, z-directions (confirmed by the correlation lengths: $L \approx L_x \approx L_y \approx L_z$). Thus, the studied soil material (Fig. 7a) can be considered as an isotropic material which is consistent with the method used to prepare it. The opportunity to discuss the anisotropy along particular directions across the basic grains assemblage should enable the study of how soil processes affect porosity at the scale of these basic grains.

Due to digitising, the smallest voids (or solids) described were poorly defined and did not correspond to real objects. Thus, for chord lengths (r) such as $r < 3$ pixels, chord distributions exhibited a linear increase that had no basis in reality and thus did not have to be taken into account (Levitz and Tchoubar, 1992; Rozenbaum et al., 2007). As shown in Fig. 9, void and solid chord distributions exhibited an exponential decrease. This type of porous medium, in which both the void and solid chord distributions are exponential, is called a long-range random medium (Debye et al., 1957; Levitz and Tchoubar,

1992). Thus, the void and solid phases in the image were randomly distributed for chord length ranging from 3 to 80 μm and from 3 to 120 μm, respectively (Fig. 9). The lack of longer chords within the 3D image 588 μm in diameter and 716.8 μm high indicates the lack of void and solid volume with a size larger than 80 and 120 μm in all directions, respectively. The lack of correlation peaks demonstrates that the size distribution of void and solid phases were homogeneously distributed, thus indicating the lack of a particular size for the void and solid phase volumes within the range of recorded chord lengths. In the case of such an exponential decay, l_v is the persistence length for the void phase and l_s is the persistence length for the solid phase. These two persistence lengths correspond to mean distances between two interfaces across the void and solid phases, respectively. The mean first moments of the chord distributions were l_v = 6.9 μm and l_s = 13.4 μm. Cousin et al. (1996) considered that a 3D cubic image is a representative volume when its side is greater than four

Table 1
Characteristics of the silt-clay material studied determined by analyzing the 3D image: l_v and l_s, first moment of the chord distribution recorded for the void and solid phase, respectively; L, correlation length; χ_v, specific Euler-Poincaré number.

Tableau 1
Caractéristiques du matériau limono-argileux étudié, obtenues par analyse de l'image 3D : l_v et l_s, premier moment de la distribution de corde enregistrée pour les phases vide et solide, respectivement ; L, longueur de corrélation, χ_v, nombre spécifique d'Euler-Poincaré.

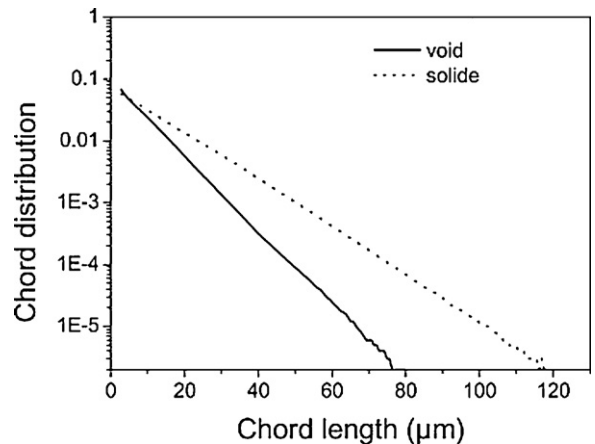| Porosity	l_v (μm)	l_s (μm)	L (μm)	χ_v (mm^{-3})
0.337	6.9	13.4	4.4	−76,792

Fig. 9. Chord distributions recorded for the studied soil material.

Fig. 9. Distributions de cordes enregistrées pour le matériau de sol étudié.

times the longest persistence length (i.e. 53.6 μm). On the other hand, we found a representative elementary volume of about 10^7 voxels for the porosity. This volume corresponds to a cube with a side of 215 pixels (151 μm), thus indicating that the side of the representative elementary volume would correspond to about ten times the longest persistence length instead of four times as proposed by Cousin et al. (1996).

he percolating void cluster represented 99.4% (1.6×10^8 voxels) of the total void phase. This shows that the entire void volume investigated at the resolution of voxels of $0.7 \times 0.7 \times 0.7$ μm^3 can be considered as connected. This is consistent with the results recorded in mercury porosimetry and confirms that the high pressures used for mercury intrusion do not break the clay bridges, thus creating connections between voids which are not present in the soil material (Bruand and Prost, 1987). This is confirmed by the negative values of the specific Euler-Poincaré number χ_V (Table 1). The remaining unconnected voids (0.6%) consisted of 8900 small clusters with sizes from several voxels up to 6000 voxels. These small clusters are probably mostly located along the rod sides and probably connected externally to the volume studied to the percolating cluster. However, such a connectivity recorded for a soil material with a clay content of 20% cannot be extended to soil materials with higher clay contents without further studies (Fiès and Bruand, 1998).

4. Conclusion

Our results show that high-resolution X-ray synchrotron microtomography enables visualisation and quantification of the void phase and the solid phase resulting from the assemblage of silt grains with a clay phase. X-ray synchrotron microtomography showed the isotropy of the silt-clay assemblage in the soil material studied. The void and solid phase volumes were smaller than 80 and 120 μm in all directions, respectively. The mean distance between two interfaces was 6.9 and 13.4 μm for the void and solid phase, respectively. X-ray synchrotron microtomography of the studied soil material also showed that the voids resulting from the assemblage of the silt grains with the clay phase can be considered as fully connected in the studied dried materials. Future work will be focussed on the separation of the clay phase and silt grains, and on soil materials at different water potentials. The data recorded will be compared with those provided by indirect methods such as the data originating from the water retention curve. The X-ray microtomography does not only enable the study of wet soil material but will enable also the discussion of the location of water in the lacunar voids such as those analysed in this study and in larger voids such as biological voids or inter-aggregates voids.

Acknowledgements

References

Acharya, T., Ray, A.K., 2005. Image Processing: Principles and Applications. Wiley-Interscience, New-Jersey, 452 p.

Attou, F., Bruand, A., 1998. Experimental study of "fragipans" formation in soils. Role of both clay dispersion and wetting-drying cycles. C.R. Acad. Sci. Paris, Ser. IIa 326, 545–552.

Attou, F., Bruand, A., Le Bissonnais, Y., 1998. Effect of clay content and silt-clay fabric on aggregate stability of artificial aggregates. Eur. J. Soil Sci. 49, 569–577.

Basile, A., d'Urso, G., 1997. Experimental corrections of simplified methods for predicting water retention curves in clay-loamy soils from particle-size distribution. Soil Technology 10, 261–272.

Biswal, B., Manwart, C., Hilfer, R., Bakke, S., Øren, P.E., 1999. Quantitative analysis of experimental and synthetic microstructures for sedimentary rock. Physica A 273, 452–475.

Braudeau, E., Bruand, A., 1993. Détermination de la courbe de retrait de la phase argileuse à partir de la courbe de retrait établie sur échantillon de sol non remanié. Application à une séquence de sols de Côte-d'Ivoire. C.R. Acad. Sci. Paris, Ser. II 316, 685–692.

Bruand, A., Prost, R., 1987. Effect of water content on the fabric of a soil material: an experimental approach. J. Soil Sci. 38, 461–472.

Bruand, A., Tessier, D., 2000. Water retention properties of the clay in soils developed on clayey sediments: significance of parent material and soil history. Eur. J. Soil Sci. 51, 679–688.

Bruand, A., Cousin, I., Nicoullaud, B., Duval, O., Bégon, J.C., 1996. Backscattered electron scanning images of soil porosity for analysing soil compaction around roots. Soil Sci. Soc. Amer. J. 60, 895–901.

Bushberg, J.T., Seibert, J.A., Leidholdt, E.M., Boone, J.M., 2006. The Essential Physics of Medical Imaging. Lippincott Williams & Wilkins, Philadelphia, 280 p.

Coulon, E., Bruand, A., 1989. Effects of compaction on the pore space geometry in sandy soils. Soil Tillage Res. 15, 137–152.

Cousin, I., Levitz, P., Bruand, A., 1996. Three-dimensional analysis of a loamy-clay soil using pore and solid chord distributions. Eur. J. Soil Sci. 47, 439–452.

Debye, P., Anderson, H.R., Brumberger, H.J., 1957. Scattering by an inhomogeneous soild. II. The correlation function and its application. J. Appl. Phys. 28, 679–683.

Fiès, J.C., Bruand, A., 1990. Textural porosity analysis of a silty clay soil using pore volume balance estimation, mercury porosimetry and quantified backscattered electron scanning image (BESI). Geoderma 47, 209–219.

Fiès, J.C., Bruand, A., 1998. A. Particle-size distribution and organization of the textural porosity: study of clay-silt-sand mixtures. Eur. J. Soil Sci. 49, 557–567.

Frykman, P., Rogon, T.A., 1993. Anisotropy in pore networks analyzed with 2-D autocorrelation (variomaps). Comput. Geosci. 19, 887–930.

Gelard, D., 2005. Identification et caractérisation de la cohésion interne du matériau terre dans des conditions naturelles de conservation. Doctorat Institut Polytechnique de Grenoble, 162p.

Hoshen, J., Kopelman, R., 1976. Percolation and cluster distribution. I. Cluster multiple labeling technique and critical concentration algorithm. Phys. Rev. B 14, 3438.

Ioannidis, M.A., Kwiecien, M.J., Chatzis, I., 1996. Statistical analysis of the porous microstructure as a method for estimating reservoir permeability. J. Petrol. Sci. Eng. 16, 251–261.

Lamotte, M., Bruand, A., Humbel, F.X., Herbillon, A.J., Rieu, M., 1997a. A hard sandy-loam soil from Northern Cameroon. I. Fabric of the groundmass. Eur. J. Soil Sci. 48, 213–225.

Lamotte, M., Bruand, A., Pédro, G., 1997b. Tendance à la lapidification de sols sableux (Hardé du Nord-Cameroun) : une évolution naturelle sous climat semi-aride à fort pouvoir évaporant. C.R. Acad. Sci. Paris Ser. IIa 325, 577–584.

Lee, S.S., Gantzer, C.J., Thompson, A.L., Anderson, S.H., Ketcham, R.A., 2008. Using high-resolution computed tomography analysis to characterize soil-surface seals. Soil Sci. Soc. Amer. J. 72, 1478–1485.

Le Trong, E., Rozenbaum, O., Rouet, J.L., Bruand, A., 2008. A simple methodology to segment X-ray tomographic images of a multiphasic building stone. Image Anal. Stereol. 27, 175–182.

Levitz, P., Tchoubar, D., 1992. Disordered porous solids: from chord distribution to small angle scattering. J. Phys. I 2, 771–790.

Macedo, A., Crestana, S., Vaz, C.M.P., 1998. X-ray microtomography to investigate thin layers of soil clod. Soil Tillage Res. 49, 249–253.

Nowamooz, H., Masrouri, F., 2010. Influence of suction cycles on the fabric of compacted swelling soil. C. R. Geoscience 342, 901–910.

Otsu, N., 1979. A threshold selection method from gray-level histograms. IEEE Trans. Sys. Man. 9, 62–66.

Ould Mohamed, S., Bertuzzi, P., Bruand, A., Raison, L., Bruckler, L., 1997. Field evaluation and error analysis of soil water content using capacitance and neutron probes. Soil Sci. Soc. Amer. J. 61, 399–408.

Papadopoulos, A., Bird, N.R., Whitmore, A.P., Mooney, S.J., 2009. Investigating the effects of organic and conventional management on soil aggregate stability using X-rays computed tomography. Eur. J. Soil Sci. 60, 360–368.

Peth, S., Horn, R., Beckmann, F., Donath, T., Fischer, J., Smucker, A.J.M., 2008. Three-dimensional quantification of intra-aggregate pore-space feature using synchrotron-radiation-based microtomography. Soil Sci. Soc. Amer. J. 72, 897–907.

Rozenbaum, O., Le Trong, E., Rouet, J.L., Bruand, A., 2007. 2D-Image Analysis: a complementary tool for characterizing quarry and weathered building limestones. J. Cult. Herit. 8, 151–159.

Russ, J.C., 2002. The Image Processing Handbook, fourth ed. CRC Press, Taylor & Francis, New-Jersey, 732 p.

Santos, G.G., Silva, E.M., Marchao, R.L., Silveira, P.M., Bruand, A., James, F., Becquer, Th., 2011. Analysis of the soil physical quality on the basis of the water retention curve: validity of the S-index. C.R. Geoscience 343, 295–301.

Schrader, S., Rogasik, H., Onasch, I., Jégou, D., 2007. Assessment of soil structural differentiation around earthworm burrows by means of X-ray computed tomography and scanning electron microscopy. Geoderma 137, 378–387.

Sleutel, S., Cnudbe, V., Masschaele, B., Vlassenbroeck, J., Dierick, M., Van Hoorebeke, L., Jacobs, P., De Neve, S., 2008. Comparison of different nano- and micro-focus X-ray computed tomography set-ups for the visualization of the soil microstructure and soil organic matter. Comput. Geosci. 34, 931–938.

Stampanoni, M., Borchertb, G., Wyssc, P., Abelab, R., Pattersonb, B., Huntb, S., Vermeulenb, D., Ruegseggera, P., 2002. High resolution X-ray detector for synchrotron-based microtomography. Nuclear Instrum. Meth. Phys. Res. A 491, 2.

Stauffer, D., Aharony, A., 1992. Introduction to Percolation Theory, second ed. Taylor & Francis, London.

Taina, I.A., Heck, R.J., Elliot, T.R., 2008. Application of X-ray computed tomography to soil science: a literature review. Can. J. Soil Sci. 88, 1–20.

Thieme, J., Schneider, G., Knöchel, C., 2003. X-ray tomography of a microhabitat of bacteria and other soil colloids with sub-100 nm resolution. Micron 34, 339–344.

Tippkötter, R., Eickhorst, T., Taubner, H., Gredner, B., Rademaker, G., 2009. Detection of soil water in macropores of undisturbed soil using microfocus X-ray tube computerized tomography (μCT). Soil Tillage Res. 105, 12–20.

Viggiani, G., Lenoir, N., Bésuelle, P., Di Michiel, M., Marello, S., Desrues, J., Kretzschmer, M., 2004. X-ray microtomography for studying localized deformation in fine-grained geomaterials under triaxial compression. C. R. Mecanique 332, 819–826.

Vogel H.V., 2008. QuantIm – some useful C/C++ functions for scientific image processing. http://www.ufz.de/index.php?en=16562.

Vogel, H.V., Cousin, I., Roth, K., 2002. Quantification of pore structure and gas diffusion as a function of scale. Eur. J. Soil Sci. 53, 465–473.